

Protonation in germanium equivalents of ringwoodite, anhydrous phase B, and superhydrous phase B

SYLVIA-MONIQUE THOMAS,^{1,*} MONIKA KOCH-MÜLLER,¹ VOLKER KAHLENBERG,² RAINER THOMAS,¹ DIETER RHEDE,¹ RICHARD WIRTH,¹ AND BERND WUNDER¹

¹GeoForschungsZentrum Potsdam (GFZ), Section 4.1, Telegrafenberg, 14473 Potsdam, Germany

²Institute for Mineralogy/Petrography, University Innsbruck, Innrain 52, A-6020 Innsbruck, Austria

ABSTRACT

To gain insight into hydroxyl solubilities and possible hydration mechanisms of mantle silicates, as well as to test the utility of germanium analog models in studies of water-related defects, our present work is focused on the protonation of germanium analogs of silicates.

For this purpose Ge-analogs of ringwoodite, anhydrous phase B (anhB), and for the first time, superhydrous phase B (shyB), were synthesized in a piston cylinder device at 2 GPa and 950–1000 °C under water-excess conditions. Electron probe microanalysis (EPMA), transmission electron microscopy (TEM), and X-ray diffraction as well as Raman and infrared (IR) spectroscopy were used to characterize the experimental products.

Ge-ringwoodite incorporates from 900 to 2200 ppm H₂O by weight, which is much less than Smyth et al. (2003) observed for the Si-equivalent synthesized at 22 GPa and 1500 °C, but 200× more than published for γ -Mg₂GeO₄ by Hertweck and Ingrin (2005). In addition to this discrepancy, the incorporation mechanism of H in Ge-ringwoodite also differs from that of Si-ringwoodite.

Ge-anhB, which is currently believed to be anhydrous in the Si-system, contains from 2400 to 5300 ppm water by weight. A hydration model for germanate anhB was constructed based on single-crystal X-ray diffraction analysis and IR spectroscopy, in which OH is incorporated via the hydrogarnet substitution $[V_{\text{Ge}} \cdot 4(\text{OH})_0]^x$ and via vacant Mg sites $[V_{\text{Mg}} \cdot 2(\text{OH})_0]^x$.

For Ge-shyB the water concentration and incorporation mechanism obtained in this study are identical to results reported for the silicate phase synthesized at 22 GPa and 1200 °C (Koch-Müller et al. 2005). Thus, germanates are good low-pressure analogs for hydrous mantle silicates in which protonation is controlled by stoichiometry. However, for nominally anhydrous minerals we cannot recommend the use of germanates as high-pressure models in water-related studies. In these Ge-analogs, which are usually synthesized at much lower pressures, i.e., lower water fugacities, OH incorporation seems to differ from the high-pressure silicate equivalents qualitatively and quantitatively, as hydroxyl solubility is governed by other factors such as water fugacity and intrinsic defects.

Keywords: Germanates, ringwoodite, nominally anhydrous minerals, FTIR, anhydrous phase B, superhydrous phase B

INTRODUCTION

A significant number of high-pressure and high-temperature experiments have been carried out in the past to characterize phase relations in the system MgO-SiO₂-H₂O (MSH). Numerous investigations have established that major mantle constituents, e.g., olivine and its two dense polymorphs, are able to dissolve several wt% water, although their formulae indicate that they are nominally anhydrous minerals (NAMs) (e.g., Kohlstedt et al. 1996; Smyth 1987; Smyth et al. 1997; Kudoh et al. 2000; Bolfan-Casanova et al. 2000; Klepepe et al. 2002; Kohn et al. 2002). Cubic ringwoodite [γ -(Mg,Fe)₂SiO₄] with the space

group $Fd\bar{3}m$ is thought to be one of the most abundant minerals in the Earth's transition zone, from about 525 to 660 km depth. Therefore, the ability to store hydroxyl in its structure is of particular interest. Likewise, many dense hydrous magnesium silicates, first discovered by Ringwood and Major (1967), have been recognized that are stable at very high pressures and temperatures and cover a wide range of water and silica contents (e.g., phase D and phase E; e.g., Yamamoto and Akimoto 1974; Akaogi and Akimoto 1986; Kato and Kumazawa 1985; Kanzaki 1991; Gasparik 1993; Luth 1993; Cynn et al. 1996; Frost 1999; Ohtani et al. 2001; Ganguly and Frost 2006). One of these phases is anhB (Mg_{1.4}Si₃O₂₄) with an atomic Mg/Si ratio of 2.8. It was first synthesized at 2380 °C and 16.5 GPa by Herzberg and Gasparik (1989). Another phase in the MSH system is shyB [Mg₁₀Si₃O₁₄(OH)₄], a nominally hydrous phase with an atomic Mg/Si ratio of 3.3 and 5.8 wt% of stoichiometrically incorpo-

* Present address: Department of Earth and Planetary Sciences, Northwestern University, 1850 Campus Drive, Evanston, Illinois 60208, U.S.A. E-mail: smthomas@earth.northwestern.edu

rated water. It was first synthesized at 1450 °C and 19 GPa and described by Gasparik (1993). According to their *P-T* stabilities these dense hydrous magnesium silicates are potential hosts for water in cold subduction zones. However, whether they really exist in nature is still under debate. If they do, their dehydration in hotter parts of the lower mantle could have, among other effects, implications for as yet poorly understood deep-focus earthquakes (Silver et al. 1995). Such examples suggest the geological importance of studying the protonation of compounds in the MSH system, qualitatively and quantitatively, as water dissolved in these minerals may change their chemical and physical properties and might have an unforeseen impact on mantle processes.

To investigate such mantle silicates, germanates have been extensively used as analogs. In contrast to silicates, germanates require much lower pressures for specific phase transitions, because at zero pressure tetravalent Ge inherently has a slightly larger atomic radius than tetravalent Si. As shown by Ringwood (1975), phase transformations are controlled by critical effective radius ratios.

In recent studies, Blanchard et al. (2005a, 2005b) modeled OH defects in germanate ringwoodite and suggested using germanium analogs to study the protonation of NAMs. However, only dry Ge-anhB (e.g., Von Dreele et al. 1970) and Ge-ringwoodite, containing 5 to 10 ppm water by weight (Hertweck and Ingrin 2005) have been previously synthesized as high-pressure models. The data obtained provided useful constraints on structure, crystal chemistry, phase transformations, and *P-T* stabilities. However, the hydrogen incorporation mode in those phases is still largely unknown. The aim of this work is to test the utility of germanium analog models in studies of water-related defects, and to do this we synthesized the Ge-analogs of ringwoodite, anhB, and Ge-shyB. On the basis of X-ray refinements and IR spectra we developed new hydrogen incorporation models for Ge-ringwoodite and Ge-anhB. Furthermore, we compare our results with the associated silicon equivalents and discuss the application of germanates as low-pressure analogs.

EXPERIMENTAL METHODS

Syntheses

Starting materials were made up from MgO, Mg(OH)₂, and GeO₂ to give compositions with different MgO-GeO₂ ratios. The starting powders were loaded in 10 mm long gold capsules with an outer diameter of 6 mm and a wall thickness of 0.5 mm and were sealed by cold welding to avoid water loss. All experiments were carried out in an end-loaded piston-cylinder apparatus (Boyd and England 1960) at 2 GPa and 950 or 1000 °C with up to 23 wt% water. Starting mixtures,

experimental conditions and compositions of the run products are summarized in Table 1. After quenching, the recovered capsule was opened and checked for the presence of excess water, which was observed in all runs.

Electron probe microanalysis

For chemical analyses several grains of Ge-anhB and Ge-shyB were mounted, polished and coated with carbon. Compositions were measured with a Cameca SX-50 electron microprobe using wavelength-dispersive spectrometers with a PAP correction procedure. The microprobe was operated at 15 kV with a beam current of 20 nA and a spot size of 2 μm. Counting times were 60 s on peaks (Mg, Ge) and 30 s on backgrounds (left and right side of the peaks). Ge-ringwoodite synthesized in this study was used as the standard. This was justified by single-crystal X-ray refinement of this sample (see below).

Transmission electron microscopy

To characterize microstructures, sample homogeneities, and compositions by TEM, specific foils were prepared from single crystals mounted in crystal-bond, using the focused-ion-beam technique (Wirth 2004), and a FEI FIB200 focused ion beam device with a Ga-ion source operated with an acceleration voltage of 30 kV. Final foils of 15 × 10 × 0.2 μm in size were removed from the sample using an optical microscope and placed onto a perforated carbon TEM grid. No further carbon coating was required. TEM analyses of Ge-anhB and Ge-ringwoodite were performed in a Philips CM200 electron microscope operating at 200 kV with a LaB₆ electron source. Ge-shyB was analyzed with a FEI Tecnai G²F20 X-Twin at 200 kV equipped with a FEG electron source. Both microscopes are provided with a Gatan imaging filter for the acquisition of energy-filtered images and high-resolution electron micrographs, and an energy-dispersive X-ray spectroscopy system for analytical electron microscopy. Electron diffraction was used to determine the orientation of the samples.

X-ray diffraction

The samples were identified by polarized light microscopy and X-ray diffraction. Table 1 lists the run products with their characteristics. X-ray powder measurements on Ge-shyB were done with a fully automated STOE Stadi P diffractometer, equipped with a curved Ge (111) primary monochromator, a 7° wide position-sensitive detector (PSD) and CuKα radiation. The X-ray tube was operated at 40 kV and 40 mA, using a take-off angle of 6°. Intensities were recorded in the range of 5–125 °2θ with a detector step size of 0.1° and a resolution of 0.02°. Unit-cell parameters were determined using the GSAS software package for Rietveld refinement (Larson and Von Dreele 1987).

In addition, small platy specimens of Ge-anhB and Ge-ringwoodite were measured on a Stoe IPDS-II imaging plate diffractometer at the Mineralogical Institute of the University of Innsbruck, Austria. Parameters pertaining to the data collection and the subsequent structure refinements are summarized in Table 2. All data were numerically corrected for absorption by use of indexed crystal faces. Further data reduction including Lorentz and polarization corrections were performed with the STOE program package X-RED (X-RED 1996).

Raman spectroscopy

Raman spectra of several sample grains were taken using a Dilor XY Laser Triple 800 mm spectrometer (1800 lines/mm gratings), equipped with a Peltier-cooled CCD detector (1024 elements), a Coherent water-cooled Argon Laser, an Olympus optical microscope and a long working distance 80× objective (ULWD MSPlan80). The slit width was 100 μm at a corresponding spectral resolution

TABLE 1. Starting compositions, experimental conditions, electron microprobe analyses (wt%), and structural formulae

Sample	Starting composition (wt%)			<i>P</i> (GPa)	<i>T</i> (°C)	Run duration (h)	Characteristics
	MgO	GeO ₂	H ₂ O				
Ge-anhB	43.51	37.06	19.43	2	1000*	10	clear crystals, up to 200 μm, no coexisting phase
Ge-ringwoodite	43.51	46.77	9.72	2	950	24	clear crystals with nearly ideal cubic sections, up to 400 μm in size, no coexisting phase
Ge-shyB	51.88	24.95	23.17	2	1000	16	clear crystals of Ge-shyB, up to 50 μm in size, coexisting phases: periclase, brucite
Sample	No. anal.	MgO	GeO ₂	Total	Formula		
Ge-anhB	28	51.18(16)	48.34(47)	99.52(51)	Mg _{13.89(6)} Ge _{5.06(3)} O ₂₄		
Ge-shyB	12	51.33(24)	40.43(25)	91.77(32)	Mg _{9.96(3)} Ge _{3.02(2)} O ₁₄ (OH) ₄		

Note: Numbers in parentheses give 1σ standard deviation in terms of the preceding figure.

* Temperature between 1000 and 1100 °C.

TABLE 2. Crystal structure data and statistic parameters for Ge-ringwoodite and Ge-anhB at room temperature from single-crystal refinements

	Ge-ringwoodite	Ge-anhB
Empirical formula	$\gamma\text{-Mg}_2\text{GeO}_4$	$\text{Mg}_{14}\text{Ge}_5\text{O}_{24}$
Temperature	293(2) K	293(2) K
Wavelength	0.71069 Å	0.71069 Å
Crystal system	cubic	orthorhombic
Space group	$Fd\bar{3}m$	$Pb\bar{a}m$
Unit-cell dimensions	$a = 8.246(2)$ Å $b = 8.246(2)$ Å $c = 8.246(2)$ Å	$a = 14.52(2)$ Å $b = 10.231(16)$ Å $c = 5.947(8)$ Å
Volume	$560.7(6)$ Å ³	$884(2)$ Å ³
Z	8	2
Density (calculated)	4.388 g/cm ³	4.095 g/cm ³
Absorption coefficient	11.186 mm ⁻¹	9.053 mm ⁻¹
Theta range for data collection	4.28 to 28.55°	2.43 to 29.27°
Index ranges	$-11 \leftarrow h \leftarrow 11, -10 \leftarrow k \leftarrow 11, -11 \leftarrow l \leftarrow 11$	$-19 \leftarrow h \leftarrow 19, -14 \leftarrow k \leftarrow 14, -8 \leftarrow l \leftarrow 8$
Reflections collected	1189	7977
Independent reflections	50 [$R(\text{int}) = 0.0629$]	1307 [$R(\text{int}) = 0.0521$]
Refinement method	Full-matrix least-squares on F^2	Full-matrix least-squares on F^2
Data/restraints/parameters	50/0/8	1307/0/125
Goodness-of-fit on F^2	1.442	1.185
Final R indices [$I > 2\sigma(I)$]	$R1 = 0.0397, wR2 = 0.1436$	$R1 = 0.0354, wR2 = 0.0669$
R indices (all data)	$R1 = 0.0401, wR2 = 0.1457$	$R1 = 0.0516, wR2 = 0.0710$
Extinction coefficient	0.07(2)	0.0008(4)

Note: Numbers in parentheses give 2 σ standard deviation in terms of the preceding figure.

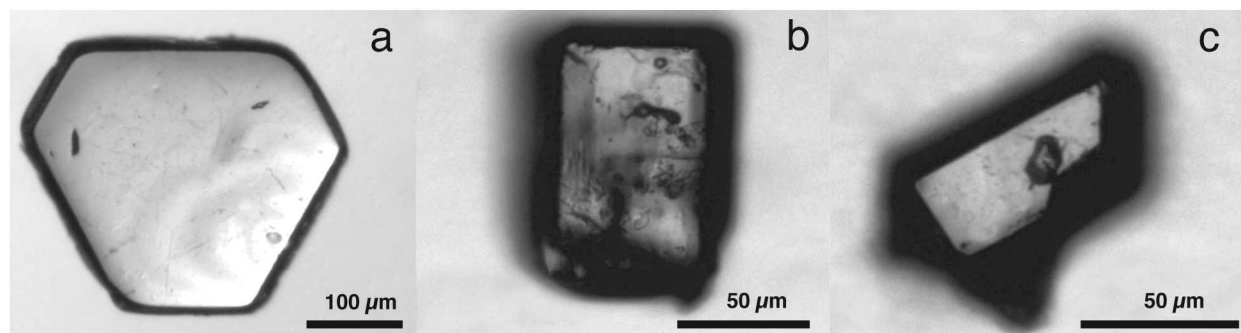


FIGURE 1. Images of (a) Ge-ringwoodite, (b) Ge-anhB, and (c) Ge-shyB crystals synthesized in this study. Black spots reflect surface contamination.

of about 1 cm⁻¹. Other spectra were acquired with a LabRAM HR800 UV-VIS spectrometer with a motorized XY-stage and a long working distance 100 \times objective (LWD VIS, NA = 0.80, WD = 3.4 mm). The 488 nm line of an Ar⁺ Laser (Model Innova 70-3) was generally used for sample excitation, at 450 and 500 mW laser power and thus 65.7 and 73 mW power on the specimen, respectively. However, the excitation source of some measurements was the 514 nm line of an air-cooled Melles Griot Ar⁺ Laser at 30 mW laser power and a power of 6.5 mW on the sample. The confocal hole of the LabRAM HR800 spectrometer was chosen according to requirements (100 to 300 μm). All spectra were recorded in two frequency ranges, high frequencies between 2800 and 4000 cm⁻¹ and low frequencies between 200 and 1400 cm⁻¹. Spectra acquisition time varied from 3 \times 10 s to 3 \times 50 s for each window.

Infrared spectroscopy

For the Fourier-transform infrared (FTIR) measurements optically clear single crystals with smooth crystal faces were selected, and dried for 18 h at 170 °C (SMT501; SMT507) or 400 °C (SMT502) in a muffle type furnace. The sample thickness was determined under an optical microscope using the eyepiece reticule and a stage micrometer scale for calibration. The final thickness ranged from 45 to 90 μm ; errors are estimated as ± 5 μm .

Unpolarized IR spectra of Ge-anhB and Ge-ringwoodite were recorded from room temperature down to -180 °C with a Bruker IFS 66v FTIR spectrometer and a Hyperion microscope, an InSb detector, a KBr beamsplitter, a globar, and a Linkam FTIR600 heating/cooling stage. The spot size used in the measurements

ranged from 50 \times 50 to 100 \times 100 μm , and up to 1024 scans were taken with a resolution of 2 cm⁻¹. To avoid detector saturation due to a strong OH absorbance, IR studies on Ge-shyB were carried out on a thin aggregate of randomly oriented sample particles, produced by crushing a crystal in a Megabar-type diamond anvil cell (DAC) (Mao and Hemley 1998) without a gasket. In situ IR spectra as a function of pressure were taken in the DAC with type II diamonds (culet sizes of 800 μm) and a stainless steel gasket. The sample was placed in a 300 μm gasket hole with KBr as pressure medium and ruby grains. For each spectrum 1024 scans were accumulated in the range of 400–4000 cm⁻¹ with a KBr beam splitter, a MCT detector and 2 cm⁻¹ resolution. The pressure was determined using the pressure-dependent energy shift of the R₁ ruby fluorescence line (Mao et al. 1986). High-pressure spectra for the other two samples were collected on single crystals under the same conditions, but in the 1850–4000 cm⁻¹ range.

Polarized IR spectra of single crystals of Ge-anhB were obtained under the above-mentioned conditions, and in addition with synchrotron radiation at the Infrared beamline at BESSY II using a Nicolet 870 FTIR spectrometer equipped with a Continuum microscope. The orientations of the samples were determined using electron diffraction patterns from TEM analyses (see results). For the polarized spectra 512 scans were collected at 4 cm⁻¹ resolution. The absorbance of the oriented single crystals was measured in extinction position, with the electric vector (**E**) parallel to each optical indicatrix axis. The integrated intensity and area-weighted average (Libowitzky and Rossman 1997) of the peak positions were obtained using the PeakFit software by Jandel Scientific. Due to the lack of specific absorption coefficients for Ge-anhB and Ge-ringwoodite, we used the calibration of Libowitzky and Rossman (1997) to quantify the hydrogen content.

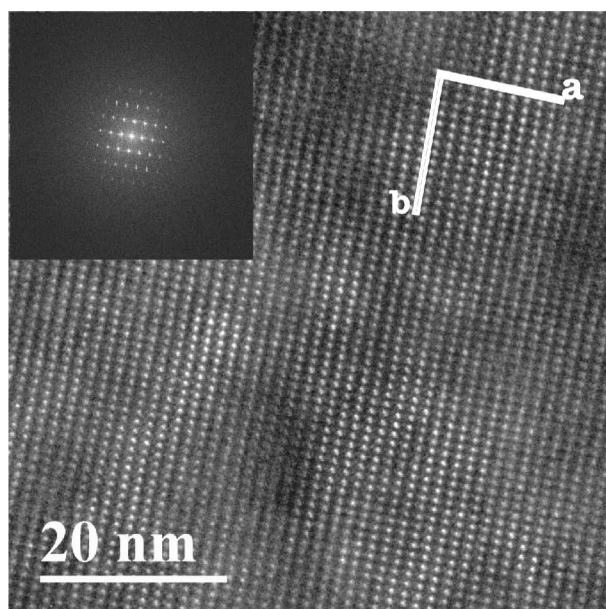


FIGURE 2. High-resolution transmission electron microscopy image and corresponding electron diffraction pattern of Ge-anhB. Lattice fringes reveal the homogeneous nature of the sample.

For Ge-anhB total absorbances were used, i.e., the sum of the fitted integrated intensities measured parallel to the three crystallographic axes. For the unpolarized spectra of γ -Mg₂GeO₄, total absorbances were calculated by multiplying the integrated absorbance by three. Synchrotron FTIR was used to study the OH distribution in the samples. Due to the high brilliance of the synchrotron beam the spatial resolution is much higher compared to a conventional light source. It was possible to obtain area maps of the OH distribution in the spectral region 2700–3800 cm⁻¹ for Ge-anhB and Ge-ringwoodite with a real resolution of 10 × 10 and 12 × 12 μm, respectively.

RESULTS

EPMA and TEM analyses

Our syntheses resulted in clear single crystals of Ge-ringwoodite, Ge-anhB, and Ge-shyB up to several hundred micrometers in size (Fig. 1; Table 1). EPM analyses yielded the chemical formulae Mg_{13.89}Ge_{3.06}O₂₄ for Ge-anhB and Mg_{9.97}Ge_{3.01}O₁₄(OH)₄ for Ge-shyB. Results are summarized in Table 1.

TEM studies allowed us to check the run products for impurities. Figure 2 is the lattice fringe image of Ge-anhB, which shows no inclusions of foreign phases, and demonstrates the nearly perfect crystal structure that could be observed in all samples in this study. From the electron diffraction pattern of Ge-anhB, we were able to determine the crystal orientation (Fig. 2) and used this information for the collection of polarized single-crystal IR spectra.

X-ray diffraction

Ge-ringwoodite. Given that there was some controversy about the cation distribution in Ge-ringwoodite in the early 1960s, the crystal structure was refined by Von Dreele et al. (1977) using powder neutron diffraction. The space group was confirmed as *Fd* $\bar{3}$ *m* with no detectable disorder on the cation sites. Hence,

Ge-ringwoodite, isostructural with γ -Mg₂SiO₄, has a true spinel structure. Each oxygen atom is bonded to one Ge and three Mg atoms. The structure consists of two alternately stacked layers, OT (MgO₆ octahedra and GeO₄ tetrahedra) and O (MgO₆ octahedra). The results of the single-crystal X-ray refinement for Ge-ringwoodite of this study are shown in Table 2. Unfortunately, no indication for site occupation of hydrogen can be extracted from the structure refinement. Atomic coordinates, equivalent isotropic and anisotropic displacement parameters, selected bond distances, and angles are available as deposit items (Supplementary Tables 1–3¹).

Ge-anhydrous phase B and Ge-superhydrous phase B.

The crystal structures of the members of the phase B series are closely related (Finger et al. 1989, 1991). They consist of an ordered intergrowth of three layers, double OT layers (MgO₆ octahedra and TO₄ tetrahedra) alternate along the crystallographic *b* axis with O layers (MgO₆ and TO₆). The members of the phase B series all contain both tetrahedrally and octahedrally coordinated silicon atoms, which in turn are strictly segregated into distinct structural elements (Pacalo and Parise 1992). Finger et al. (1991) demonstrated that anhB crystallizes in space group *Pmcb*. The diffraction symmetry of the crystal investigated in this study was consistent with Laue group *mmm*. An analysis of the systematic absences indicated the diffraction symbol *mmmPba*-. The structure could be solved in the centrosymmetric space group *Pbam* (Table 2) using the program SIR97 (Altomare et al. 1999). Least-squares refinements were performed with the program SHELXL-97 (Sheldrick 1997). Neutral atomic scattering factors and anomalous-dispersion corrections were taken from the *International Tables for X-ray Crystallography* (Ibers and Hamilton 1974). Final calculations using anisotropic displacement parameters for all atoms converged at *R*₁ = 0.0354. The largest shift in the last cycle for these refinements was <0.001. The atomic positions obtained correspond well with those reported by Von Dreele et al. (1970) for Ge-anhB, so for better comparison, all positions were re-labeled in accordance with the earlier study. However, all lattice parameters are slightly larger than those given in Finger et al. (1991) due to substitution of Ge⁴⁺ for Si⁴⁺ (Table 3). Results of the refinement are given in Table 2. The final atomic coordinates, equivalent isotropic and anisotropic displacement parameters, as well as selected bond

¹ Deposit item AM-08-045, Supplementary Tables 1–11. Deposit items are available two ways: For a paper copy contact the Business Office of the Mineralogical Society of America (see inside front cover of recent issue) for price information. For an electronic copy visit the MSA web site at <http://www.minsocam.org>, go to the American Mineralogist Contents, find the table of contents for the specific volume/issue wanted, and then click on the deposit link there.

TABLE 3. Lattice parameters of Si-anhB compared to Ge-anhB

Lattice parameters	Si-anhydrous phase B (Finger et al. 1991)	Ge-anhydrous phase B (Von Dreele et al. 1970)	Ge-anhydrous phase B (this study)
<i>a</i> (Å)	5.868(1)*	5.944(1)	5.947(8)
<i>b</i> (Å)	14.178(1)	14.512(2)	14.52(2)
<i>c</i> (Å)	10.048(1)	10.219(2)	10.231(16)

* Numbers in parentheses are the estimated standard deviation in the preceding figure.

distances and angles can be found as Supplementary Tables 1 and 4–6¹. Crystal structure refinements showed no significant deviation from full occupancy for the Ge sites. However, for the Mg2-Mg6 sites inclusive, an occupancy slightly less than one may indicate the possible presence of vacancies (13.88 Mg per formula unit instead of 14.00), which moreover is in conformity with the formula deduced from EPMA (Table 1). In contrast, an occupancy slightly more than one was observed for the Mg1 site that could indicate the incorporation of Ge (Supplementary Table 1). Difference Fourier synthesis identified a potential hydrogen position (0.2963 0.0003 0.0000), associated with O3. That would imply a vacant Ge2 site, although not identified as such in the structure refinement.

Pacalo and Parise (1992) refined the crystal structure of shyB, and assigned it to the orthorhombic centrosymmetric space group *Pnmm*, with H in just one general position (multiplicity 8), consistent with the proposed formula ($Z = 2$). Koch-Müller et al. (2005) showed that shyB exists in at least two modifications: (1) a disordered high-temperature polymorph that crystallizes in the centrosymmetric space group *Pnmm*, and (2) an ordered low-temperature polymorph that crystallizes in the acentric space group *Pnn2*. In the low-temperature polymorph, there are two different H positions (multiplicity 4), consistent with the proposed formula ($Z = 2$), and the results from IR and Raman spectroscopy. Whereas the centrosymmetric phase exhibits one OH band (IR and Raman) and nine lattice modes in the Raman spectra, the acentric phase reveals two OH bands (IR and Raman) and 22 lattice modes in the Raman spectra (Koch-Müller et al. 2005).

First attempts to investigate single crystals of Ge-shyB by X-ray diffraction failed due to twinning of the crystals, which has also been observed for the Si-analog (Koch-Müller et al. 2005). To resolve this problem, we used X-ray powder diffraction and Rietveld refinement, and, as the basis for the crystal structure refinement for Ge-shyB, we took the structure data of the LT polymorph of shyB according to Koch-Müller et al. (2005), i.e., the space group *Pnn2*. This was justified by the presence of two OH bands in the IR spectra (see above). From the X-ray diffraction perspective, the distinction between space group *Pnmm* and *Pnn2* cannot be made from powder diffraction data. However, taking into account vibrational data for our sample (2 OH bands and 23 lattice modes), we refined the structure in analogy to the silicate equivalent, also in the space group *Pnn2*. Otherwise the existence of the two OH bands and the high number of lattice bands in our Raman spectra (cf. Raman section) cannot be explained. Results of the refinement are given in Supplementary Tables 7–9¹.

Raman spectroscopy

Room-temperature and -pressure single-phase Raman spectra of Ge-ringwoodite, Ge-anhB, and Ge-shyB are given in Figure 3. A comparison of lattice vibrations of germanates studied herein with those previously reported for the silicate equivalents is compiled in Table 4. For the germanates, a significant band shift to lower frequencies (Table 4) can be noted, caused by the substitution of tetravalent silicon by tetravalent germanium.

For pure end-member γ -Mg₂SiO₄ (McMillan and Akaogi 1987; Chopelas et al. 1994) modes at 302, 372, 600, 796, and

835 cm⁻¹ have been reported. From the site group analysis of γ -Mg₂SiO₄, the five Raman bands are due to antisymmetric and symmetric stretching vibrations of the isolated SiO₄ tetrahedron (Chopelas et al. 1994). However, previous studies also suggest that the lowest-frequency mode may be associated with octahedral cation motions (McMillan and Akaogi 1987; Chopelas et al. 1994). By analogy, the Raman spectrum of Ge-ringwoodite consists of five Raman modes at 213, 342, 521, 671, and 779 cm⁻¹ (Fig. 3b). These bands show excellent correspondence with those of previous workers (e.g., Ross and Navrotsky 1987). According to earlier studies the bands at 520, 669, and 777 cm⁻¹ derive from bending and stretching motions of the GeO₄ tetrahedron (Jeanloz 1980; Guyot et al. 1986; Ross and Navrotsky 1987). For the two low-frequency bands no unique mode specification currently exists, however, by analogy to Si-ringwoodite MgO₆ octahedral modes are highly probable (e.g., Ross and Navrotsky 1987).

In the OH stretching region, Ge-ringwoodite reveals sharp features at 3747, 3677, and 3550 cm⁻¹ and a broad band with the maximum at ~3210 cm⁻¹ which may be related to OH stretching vibrations in the crystal structure (Fig. 3a).

Raman modes attributed to lattice vibrations in Ge-anhB are shown in Figure 3d. In the high-frequency range (Fig. 3c), Raman modes caused by OH stretching vibrations at 3369, 3415, 3498, and 3591 cm⁻¹ can be detected. This is surprising, as, thus far, Si-anhB has not been considered to store traces of hydrogen (e.g., Ohtani et al. 2001; Smyth 2006). Our spectrum suggests that incorporation of water in Ge-anhB is much higher than previously reported for the Si phase.

In the Raman spectrum of Ge-shyB, we observe 23 lattice vibrations in the low-frequency range (Fig. 3f). In the Si analog peaks between 645 and 730 cm⁻¹ have been previously assigned to bending of Si octahedra, and bands between 800 and 1000 cm⁻¹ to Si-O stretching vibrations of the SiO₄ tetrahedra (Cynn et al. 1996). The high-frequency Raman spectrum of Ge-shyB is characterized by two OH stretching vibrations at 3406 and 3351 cm⁻¹ (Fig. 3e). This is in agreement with earlier vibrational studies of the low-temperature polymorph of Si-shyB (Cynn et al. 1996; Ohtani et al. 2001; Koch-Müller et al. 2005), which exhibits OH bands at 3414 and 3353 cm⁻¹.

Infrared spectroscopy

Ge-ringwoodite. The unpolarized single-crystal IR spectrum of γ -Mg₂GeO₄ (Fig. 4a) at ambient conditions consists of several OH bands, probably due to different hydroxyl groups in the structure (cf. Discussion). In the region from 3800 to 3000 cm⁻¹, we observe at least five OH bands: four at relatively high wavenumbers 3742, 3688, 3650, 3548 cm⁻¹ and one much broader band at 3207 cm⁻¹. Whereas the normalized absorbances of the high-frequency bands are more or less equal from grain to grain, those of the broad band at 3207 cm⁻¹ with a full-width at half maximum (FWHM) of 230 cm⁻¹ are highly variable (Fig. 4). Additional weak bands are indicated by small shoulders at 3531 and 3345 cm⁻¹. Low-temperature IR spectra down to -180 °C (Fig. 4b) show that with decreasing temperature the OH band at 3742 cm⁻¹ shifts 16 cm⁻¹ to higher energies (3758 cm⁻¹) (Fig. 4b, Supplementary Table 10), whereas the band at 3688 cm⁻¹ is almost insensitive (+3 cm⁻¹). Bands that are not resolved under ambient conditions are separated upon cooling. Additional OH

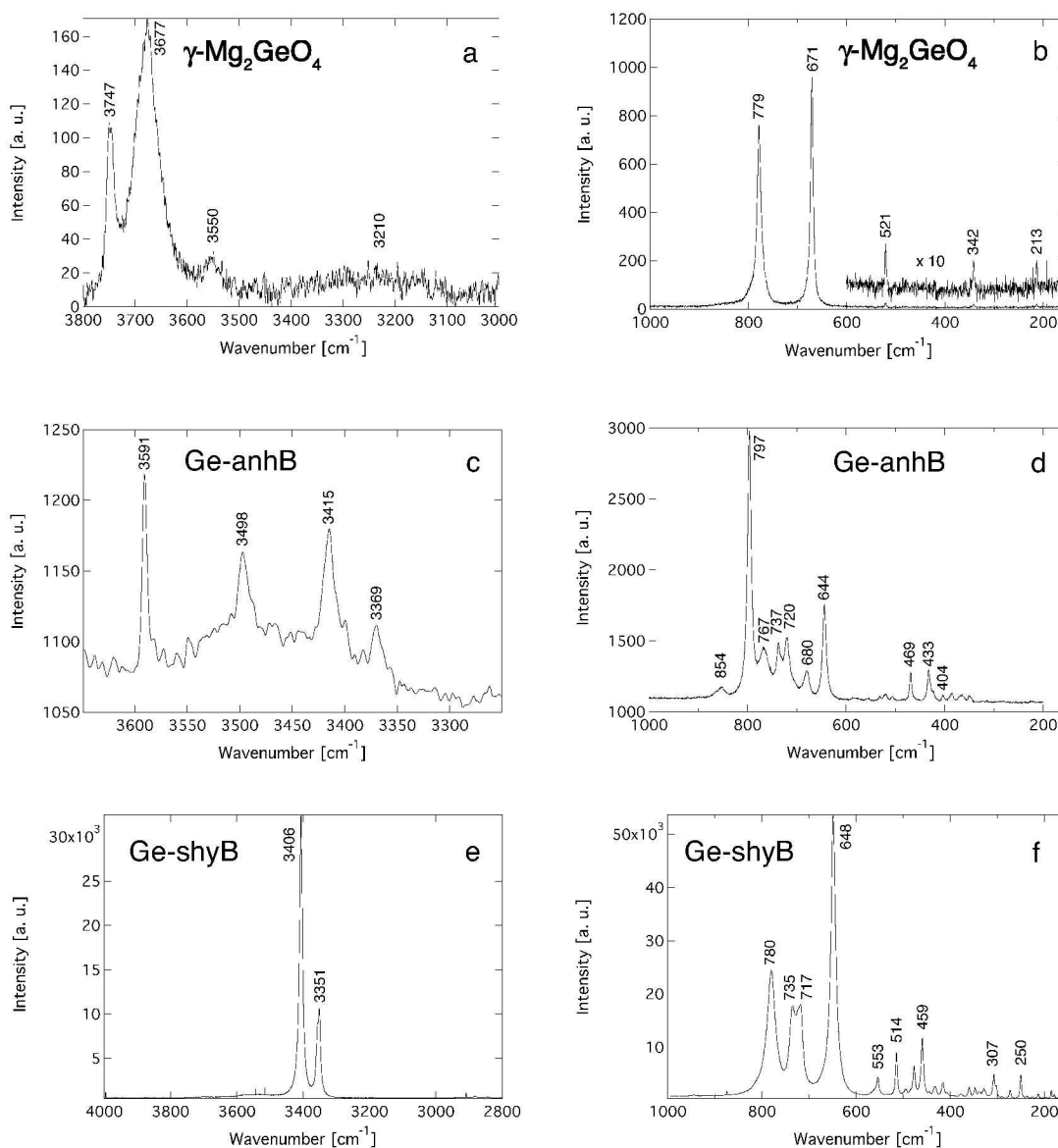


FIGURE 3. Single-crystal Raman spectra of γ - Mg_2GeO_4 (a, b) Ge-anhB (c, d), and Ge-shyB (e, f). (a) High-frequency range of γ - Mg_2GeO_4 showing modes caused by OH-stretching vibrations. (b) The Raman spectrum of γ - Mg_2GeO_4 reveals five lattice modes. In the upper spectrum, the low-energy modes are plotted at 10 \times magnification. (c, d) High- and low-frequency range of Ge-anhB. (e) OH bands and (f) lattice modes of Ge-shyB.

bands could be observed in the spectral region around 3540 cm^{-1} . Furthermore, low-temperature spectra (Fig. 4b; Supplementary Table 11) imply that the band with the center at 3207 cm^{-1} is composed of at least 2 single OH bands (3240 and 3170 cm^{-1}); a third band is indicated by a shoulder at 3345 cm^{-1} .

Ge-anhydrous phase B. Single-crystal IR spectra (Figs. 5 and 6) of Ge-anhB confirm the presence of OH groups in the structure. IR spectra show absorption bands due to fundamental OH stretching vibrations in the region from 3650 to 3200 cm^{-1} : ν_1 (3621 cm^{-1}), ν_2 (3592 cm^{-1}), ν_3 (3582 cm^{-1}), ν_4 (3497 cm^{-1}), ν_5 (3418 cm^{-1}), and ν_6 (3368 cm^{-1}). In addition two weak bands at 3613 and 3450 cm^{-1} are observed in the spectra. All crystals studied show uniform features but with varying intensities. For the

majority of the crystals the integral absorbance of the bands ν_5 and ν_6 make up $\sim 50\%$ of the observed total IR absorbance (Figs. 6 and 7). However, in exceptional cases those bands constitute only a minor component (Fig. 5), although the reason for this is unclear. Polarized IR spectra show a strong pleochroic behavior of the OH bands (Fig. 5), e.g., ν_1 reveals the strongest intensity with E parallel to the crystallographic a axis. Low-temperature IR spectra show neither band splitting nor band sharpening, but distinctive small mode shifts (up to 4 cm^{-1}) of the bands ν_1 – ν_3 , ν_5 , and ν_6 to higher energies (Fig. 6) can be observed. OH stretching band ν_4 exhibits a positive band displacement of $+11\text{ cm}^{-1}$. Upon compression all previously observed OH stretching vibrations, apart from the weak bands at 3613 and 3450 cm^{-1} ,

TABLE 4. Raman peak positions for lattice vibrations prominent in silicates and their Ge-analogs

γ -Mg ₂ SiO ₄ (McMillan and Akaogi 1987; Chopelas et al. 1994)	γ -Mg ₂ GeO ₄ (Ross and Navrotsky 1987)	γ -Mg ₂ GeO ₄ This study	Si-anhB (Ohtani et al. 2001)	Ge-anhB This study	Si-shyB (Hofmeister et al. 1999)	Si-shyB (Ohtani et al. 2001)	Ge-shyB This study
835	777	779	1025	853	1096	847sh	780
796	669	671	953	797	832	834	735
600	520	521	898	767		755	717
372	341	342	876	738	682	684	648
302	213	213	846	730sh	603	606	553
			824	720	589	590w	514
			724	680	577	555	494
			687	530w	534	537	477
			647	520w	495	504	459
			617	506w	455	481w	433
			593	469	432	434	416
			523	432	405	406w	377w
			477	423sh	365	368w	360
			465	404	337	344	347
			443	386	329		338
			410	366	309		328
			393	349	288		307
			366		276	279	302sh
			348		259		273
			336			231	250
			310		222		213w
			255		212		186
			219				171w

Note: All frequencies are given in cm⁻¹; "sh" indicates shoulder; "w" indicates weak.

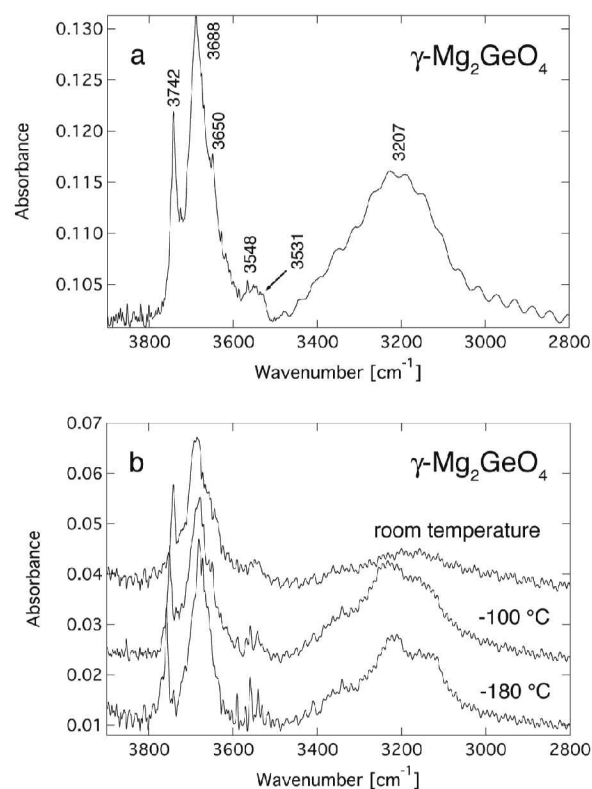


FIGURE 4. (a) Unpolarized IR spectrum of a 53 μm thick single crystal of Ge-ringwoodite and (b) of a 73 μm thick single crystal, as a function of temperature. The spectra are offset for clarity.

are resolvable (Fig. 7). We observe a negative mode shift of all vibrations, and a slight broadening of the bands with increasing pressure (Fig. 7; Supplementary Table 11). The highest peak position displacements are displayed by v2 and v6, with -27

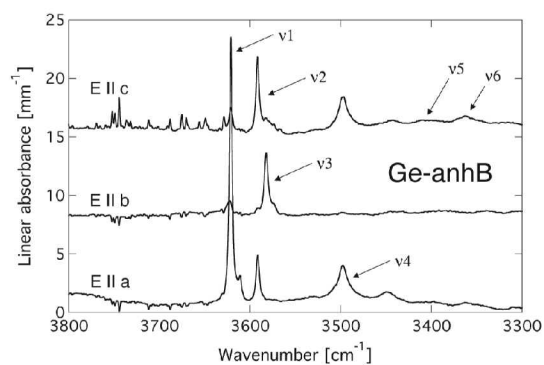


FIGURE 5. Polarized IR spectra of Ge-anhB recorded with synchrotron radiation with E parallel to a , b , and c demonstrating the strong pleochroism of the OH bands. The spectra are offset for clarity.

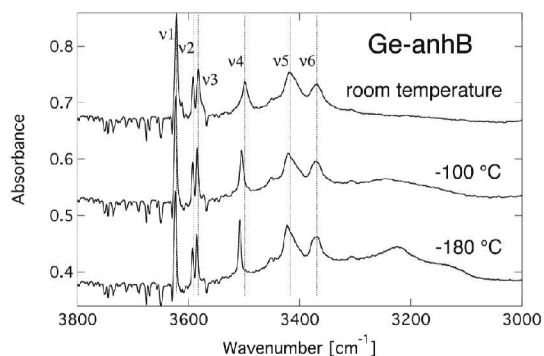


FIGURE 6. Unpolarized low-temperature IR spectra of a 61 μm thick single crystal of Ge-anhB down to -180°C . The spectra are offset for clarity.

and -39 cm^{-1} , respectively.

Ge-superhydrous phase B. The IR spectrum of Ge-shyB (Fig. 8) shows two OH stretching bands at 3404 cm^{-1} (v1) and

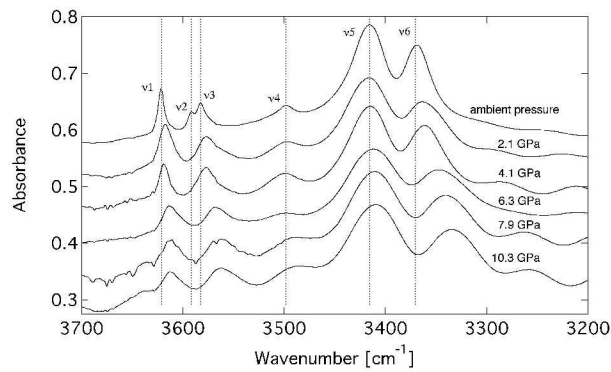


FIGURE 7. Pressure-dependent IR spectra of a 45 μm thick single crystal of Ge-anhB determined in a DAC. The spectra are offset for clarity.

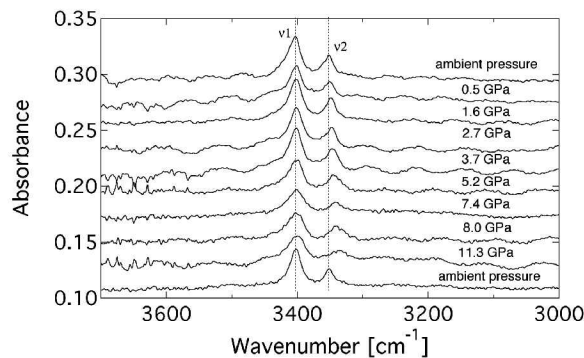


FIGURE 8. Pressure-dependent IR spectra of Ge-shyB recorded in a DAC. The lower ambient pressure spectrum has been recorded after pressure release. The spectra are offset for clarity. The thickness of the thin aggregate analyzed is estimated to be $<5 \mu\text{m}$.

3353 cm^{-1} (v2). With increasing pressure a shift of v2 to lower energies (-16 cm^{-1}) and a minor increase in FWHM of $\sim 3 \text{ cm}^{-1}$ can be observed in the spectra. In contrast, v1 position and FWHM do not change significantly with increasing pressure (Fig. 8). Both bands have been previously reported for Si-shyB (Cynn et al. 1996; Koch-Müller et al. 2005).

OH distribution and quantification

Unpolarized IR maps of Ge-ringwoodite and Ge-anhB of regions of equal thickness confirm the assumption that hydroxyl groups are homogeneously distributed in the crystal structure. However, as previously mentioned the defect concentration may vary from crystal to crystal.

Table 5 lists the total integrated absorbances of the hydroxyl bands obtained by fitting the unpolarized (Ge-ringwoodite) and polarized (Ge-anhB) IR spectra. Water contents of Ge-ringwoodite and Ge-anhB range from 900 to 2200 wt ppm H_2O and from 2400 to 5300 wt ppm H_2O , respectively (Table 5), depending on the proportions of low-frequency OH bands in the spectra. In contrast to the above-mentioned samples Ge-shyB is a hydrous phase in which H is incorporated by stoichiometry. According to its chemical formula $\text{Mg}_{10}\text{Ge}_3\text{O}_{14}(\text{OH})_4$ it contains 4.8 wt% water. Simply taking the difference from 100% in the microprobe analyses totals as wt% H_2O would indicate a higher amount of water (Table 1), however higher water concentrations would require additional H positions, and there is no indication of such a deviation from stoichiometry, either from IR spectroscopy or from the X-ray refinement. Moreover, the difference from 100% in microprobe analysis reflects water concentration plus total experimental error, so will be affected by other errors in the sample preparation or measurement procedure. However, despite the low total sum obtained by EPMA the chemical formula could be calculated correctly on the basis of 14 O^{2-} and 4 OH^- . Therefore, we assume the water content of Ge-shyB to be analogous to the Si-phase at least to the same order of magnitude.

DISCUSSION

Ringwoodite

Hertweck and Ingrin (2005) report much lower water contents (5–10 wt ppm) for $\gamma\text{-Mg}_2\text{GeO}_4$, than those observed in this study, although those authors conducted their synthesis under similar P - T conditions. Their IR spectra are also quite different from those of this study, as they consist of only one band at 3531 cm^{-1} , with a shoulder at 3502 cm^{-1} . A possible explanation for the significant differences in the water concentration and incorporation mechanism between the two samples would be that the experiment by Hertweck and Ingrin (2005) was water undersaturated. Compared to pure $\gamma\text{-Mg}_2\text{SiO}_4$, storing up to $\sim 2.2 \text{ wt}\% \text{ H}_2\text{O}$ (e.g., Inoue et al. 1998), Ge-ringwoodite samples synthesized at

TABLE 5. Estimated water contents from IR spectra of Ge-anhB and Ge-ringwoodite

Sample	No. of IR measurements	ϵ ($\text{Lcm}^2/\text{mol}_{\text{H}_2\text{O}}$)	Water content (wt ppm H_2O)	A_{tot} (mm^{-1})	Density (g/cm^3)	Peak position (cm^{-1})†
Libowitzky and Rossman (1997)						
Ge-anhB	4	40689	5313	4918	4.10	3588*
		63130	2433	3494	4.10	3497
		69889	3336	5304	4.10	3470
		70557	3710	5955	4.10	3467
Ge-ringwoodite	6	47962	2049	2402	4.39	3559‡
		82581	1579	3187	4.39	3418‡
		33538	1727	1416	4.39	3617‡§
		65433	1926	3081	4.39	3488‡
		34771	2195	1866	4.39	3612‡§
		56225	904	1242	4.39	3525‡

* v5 and v6 not observed in IR spectra.

† The area-weighted average of the peak positions is used as suggested by Libowitzky and Rossman (1997).

‡ The standard deviation of the peak position reflects grain-to-grain intensity differences of the broad band at $\sim 3200 \text{ cm}^{-1}$.

§ Peak position reflects minor contributions of the broad band at $\sim 3200 \text{ cm}^{-1}$.

much lower pressures in this study show a much lower water concentration and different hydration mechanisms.

The main feature in the IR spectrum of pure γ - Mg_2SiO_4 , synthesized at 22 GPa and 1500 °C, is a broad band (FWHM \sim 530 cm^{-1}) at 3105 cm^{-1} (e.g., Smyth et al. 2003). However, additional weaker bands at about 3645 cm^{-1} (Kohlstedt et al. 1996), 3668 cm^{-1} (Chamorro-Pérez et al. 2006), or 3685 cm^{-1} (Kudoh et al. 2000) have been reported for hydrous magnesian ringwoodite, synthesized at lower pressures and temperatures (19–19.55 GPa and 1100–1300 °C).

Both, Mg- and Si-vacancies have been proposed for the incorporation of hydroxyl groups in the ringwoodite structure (Kohlstedt et al. 1996; Kudoh et al. 2000; Smyth et al. 2003, 2004; Hertweck and Ingrin 2005; Blanchard et al. 2005a, 2005b; Chamorro-Pérez et al. 2006). From single-crystal X-ray studies Smyth et al. (2003) suggest the protonation of an octahedral site for pure γ - Mg_2SiO_4 . However, they also state that the absorption feature at \sim 3105 cm^{-1} would correlate with short O-O distances of a tetrahedral site. Kohlstedt et al. (1996) and Kudoh et al. (2000) propose a small amount of cation disorder (partial occupancy of the tetrahedral site by Mg) and protonation of both tetrahedral and octahedral sites, since they observe additional OH-stretching bands at about 3645 cm^{-1} (Kohlstedt et al. 1996) and 3685 cm^{-1} (Kudoh et al. 2000), whose frequencies correlate with protonation of octahedral sites.

Blanchard et al. (2005a, 2005b) calculated similar defect energies for γ - Mg_2SiO_4 and its low-pressure analog γ - Mg_2GeO_4 using classical atomistic computer simulations, and thus imply that both compounds follow the same protonation trends. According to their models, the most favorable hydration mechanism for γ - Mg_2SiO_4 is associated with tetrahedral vacancies, namely the hydrogarnet substitution. However, in a more recent recalculation of their data (Blanchard and Wright 2006), applying density functional theory, and in consideration of mantle pressures, they now suggest hydroxyl groups prefer Mg vacancies, when entering the spinel structure. This is consistent with proposed protonation sites by Ross et al. (2003) located by studying the properties of the electron density distribution in γ - Mg_2SiO_4 .

The spinel structure in the space group $Fd\bar{3}m$ contains only one oxygen position, which must be the bonding site for hydrogen. There are four O \cdots O distances relevant in discussing the OH direction and band position. Due to the cubic symmetry, we cannot determine the OH direction from polarized IR measurements. The only evidence on which to assign OH bands to OH groups are the band positions, and the band temperature and pressure dependences. For cubic γ - Mg_2SiO_4 , the O \cdots O distance within a tetrahedral site is 2.7137 Å. The octahedra show two different O \cdots O distances, 2.8546 and 2.9922 Å. Another very long O \cdots O distance is that between an O atom of a Si tetrahedron and an O atom of a Mg octahedron, which is 3.9387 Å. From the Libowitzky (1999) model it would be convincing to assign the low-energy band to vacant tetrahedral sites, and the high-energy band to a vacant octahedral site, because the O-H \cdots O distances correlate well with the band positions. However, it has been proposed (e.g., Lager et al. 1987, 1989) that a vacant tetrahedron will expand locally with the magnitude of the expansion depending on the host. Hence, given a very large expansion, the tetrahedral edge will be longer than the octahedral edge (e.g., Lager et al.

1987, 1989). For this reason an OH band assignment to distinct sites is even more complex.

Hertweck and Ingrin (2005) propose the hydrogarnet substitution for their Ge-ringwoodite, i.e., OH incorporation coupled with a vacant tetrahedral site. They propose that the band position correlates with the GeO_4 tetrahedral edge length of \sim 2.9(1) Å. However, Hertweck and Ingrin (2005) also point out that a proton position assignment in Ge-ringwoodite is very difficult due to the fact that, unlike the silicate compound, tetrahedral and octahedral edge lengths have nearly equivalent values of \sim 2.9 Å (Von Dreele et al. 1970). The IR spectra of the Ge-ringwoodite in our study indicate at least five different OH groups. The O \cdots O distances within a tetrahedral site are 2.923 Å, within an octahedral site 2.895 and 2.909 Å, and the very long distance is 4.104 Å. From the relationship suggested by Libowitzky (1999) these distances are long, and would correlate with high-energy band positions. From the same model, the origin of the low-energy band in the Ge-analog cannot be explained. A possible cause could be that a vacant tetrahedral Ge site is much smaller than an occupied site. However, this would be opposite to that observed for silicates (Armbruster and Gnos 2000). Another option would be to interpret this broad absorption feature as molecular water, discussed by Smyth et al. (2003, 2004) for γ - Mg_2SiO_4 , but excluded by reason of a high reproducibility of the absorption signal from grain to grain and its strong correlation with unit-cell volume. In the case of Ge-ringwoodite, the incorporation of molecular water would explain the low-energy of the band and the fact that the integrated area was not highly reproducible from grain to grain. Moreover, band splitting was observed in the low-temperature IR spectra, as reported for IR spectra of ice. However, γ - Mg_2GeO_4 in this study showed no stretch-bend combination mode in the 5200 cm^{-1} region. Moreover, contrary to the generally strong mode shifts of \sim 200 cm^{-1} reported for the water-ice transition, in our sample only a small negative total band shift was found. Hence, we suggest that this band is due to a range of O-H \cdots O distances rather than molecular water. The very large FWHM of the low-energy band in Si-ringwoodite spectra could be explained as a statistical distribution of the protons among three possible H symmetry sites ($1m$ or $3m$) due to the $3m$ site symmetry of the oxygen atom (Kudoh et al. 2000). The latter specification would be consistent with our low-temperature spectra of γ - Mg_2GeO_4 in which the low-energy band splits into at least two bands with decreasing temperature (cf. IR section). Our data give no evidence that the broad band in Ge-ringwoodite is equivalent to the broad absorption signal found in γ - Mg_2SiO_4 . For example, Bolfan-Casanova et al. (2000) observe no significant change of the appearance of the broad band upon cooling to -50 °C in Si-ringwoodite. Moreover, our broad band has a smaller FWHM of 230 cm^{-1} , and, in contrast to the silicate, is only modestly reproducible from crystal to crystal. In the γ - Mg_2GeO_4 spectra from this study the high-frequency bands are the dominant features, whereas the broad band at \sim 3100 cm^{-1} is the main feature in γ - Mg_2SiO_4 . The single band at the highest energy of 3742 cm^{-1} has not been previously reported for γ - Mg_2SiO_4 . Based on its shift to even higher frequencies upon cooling, it would be a good candidate for the very long bond distance (4.104 Å), moreover, it is indicative of a very strong OH dipole, with no hydrogen bonding. The band shift to even higher energies dur-

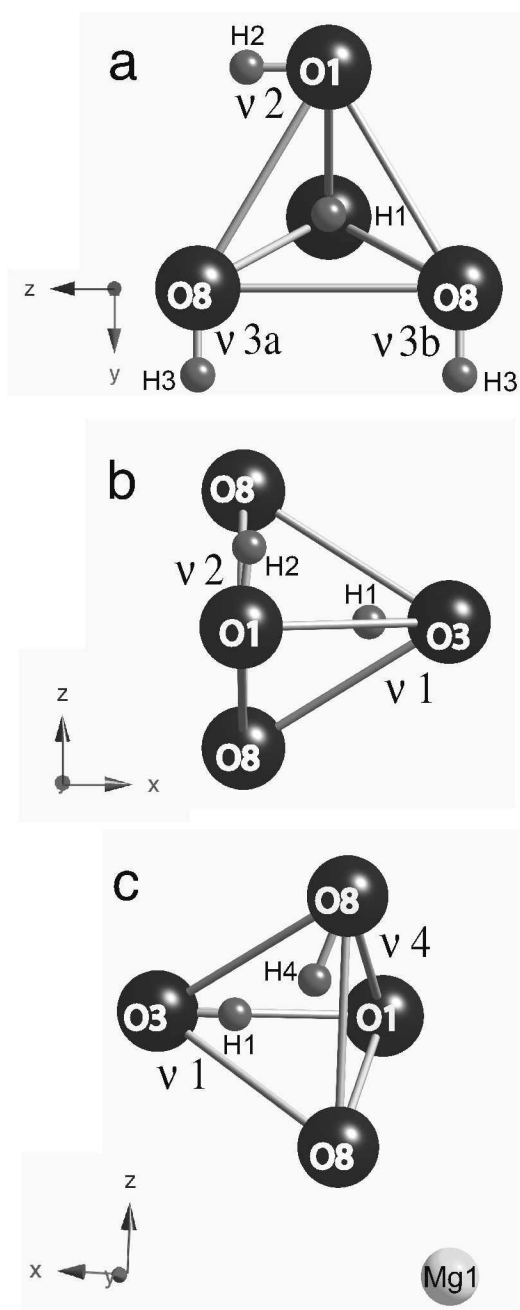


FIGURE 9. Projection of a vacant GeO_4 tetrahedron in Ge-anhB (a) parallel to (100) and (b) parallel to (010) showing defect 1. (c) Projection of atoms involved in defect 2 in Ge-anhB parallel to (010).

ing cooling supports the latter suggestion, as the OH dipole gets even stronger. The band at 3688 cm^{-1} could be due to vibration of an OH dipole occupying a vacant octahedron, pointing in the direction of the octahedral $\text{O}\cdots\text{O}$ distances (2.895 and/or 2.909 Å). In conclusion, compared to $\gamma\text{-Mg}_2\text{SiO}_4$, Ge-ringwoodite synthesized in this study contains much less “water,” and based on our observations, seems to incorporate “water” in a different way to the Si-analog.

Ge-anhydrous phase B

In contrast to previous data on anhB (e.g., Ohtani et al. 2001), our spectra of its germanium equivalent reveal the presence of OH groups in the structure. We have developed a hydration model for Ge-anhB on the basis of X-ray structure refinements and polarized IR spectra on oriented crystals. We propose two OH defects, the first defect (Figs. 9a and 9b) based on the results of X-ray structure refinement, corresponds to the hydrogarnet substitution: a vacant GeO_4 tetrahedron where four charge-compensating protons combine with the O atoms to four OH groups. These OH groups give rise to four OH stretching vibrations v1, v2, v3a, and v3b. The difference Fourier synthesis showed a potential hydrogen position H1 close to O3 (see results), which would imply a vacant Ge2 site. In contrast to models for coesite (Koch-Müller et al. 2003) or garnet (e.g., Lager et al. 1987, 1989; Libowitzky and Beran 2006) where OH dipoles involved in these defects are located outside the tetrahedron, the O3-H1 dipole suggested here points inward. Taking into account that a Ge tetrahedron is much larger than a Si tetrahedron, and that a vacant tetrahedron may expand locally (e.g., Lager et al. 1987, 1989), such a dipole pointing inward does not lead to unrealistically short $\text{H}\cdots\text{O}$ distances. The atomic position of the potential hydrogen atom from the difference map would result in an O3-H1 distance of only 0.65 Å. However, again we have to take into account that the O positions are averaged over the structure, and that real O positions for the vacant tetrahedron are different. The proposed final atom position for H1 (Table 6) therefore deviates slightly from the position taken from the Fourier synthesis, resulting in a more realistic O3-H1 distance of 0.918 Å. Vibrations of the proposed O3-H1 dipole give rise to the v1 OH band, which is in good agreement with the polarized spectra. From the pleochroic behavior, and the positions of bands v2, v3a, and v3b, we propose two additional protons labeled as H2 and H3 (Figs. 9a and 9b; Table 6).

The second defect (Fig. 9c) is most probably associated with the substitution of Mg1 by Ge^{4+} , where two charge-balancing OH groups at the adjacent vacant Ge2 tetrahedron cause vibrations v1 and v4. This assignment is based on the refined site occupancy of the Mg1 site, which is slightly larger than 1.0 (Supplementary Table 1), indicating the incorporation of Ge. Thus, the OH bands in Ge-anhB, v1, v2, v3a, v3b, and v4 can be explained by the vibration of dipoles O3-H1, O1-H2, O8-H3, and O8-H4, respectively (Figs. 5 and 7; Table 6). The proposed H positions and associated O-H distances were estimated from the polarized IR measurements, and the observed band positions, taking into account the correlation of O-H-stretching frequencies and $\text{O-H}\cdots\text{O}$ distances given in Libowitzky (1999). However, note the atomic positions and associated O-H distances are only estimates, and should not be taken as absolute values. O3-H1 (v1) dipoles are involved in both defects, reflecting the high intensity of the associated OH band in the IR spectra, and explaining the fact that only one hydrogen position was refined by X-ray diffraction.

Analyses of axial compressibilities by Crichton et al. (1999) in anhB reveal that the *c* axis is most compressible, the *b* axis is least compressible, and the *a* axis is intermediate. These authors conclude that the compression of the *a* and *c* axes is controlled by

TABLE 6. Structure data of the proposed protons in Ge-anhB at ambient conditions

Dipole corresponding OH-band	Atomic positions of protons x, y, z^*	O-H distance (\AA)*	Band position (cm^{-1})	FWHM† (cm^{-1})
O3-H1 v1	0.815 0.500 0.000	0.918	3622	5.1
O1-H2 v2	0.590 0.162 0.155	0.926	3592	4.4
O8-H3 v3a	0.586 0.823 0.249	0.980	3582	7.2
O8-H3 v3b	0.586 0.823 0.752	0.980	3582	7.2
O8-H4 v4	0.390 0.081 0.080	1.063	3497	14.8

* Atomic positions and therewith the calculated O-H distances are only rough estimates and should not be taken as absolute values. They match the dipole direction determined from the polarized measurements and the band position that decreases with increasing OH distance. Other atomic coordinates are given in Supplementary Table 1.

† FWHM calculated using peak fit software (Jandel scientific).

edge-sharing octahedra in the O layer (MgO_6 and TO_6 octahedra), which promote the rigidity. Chains of edge-sharing octahedra in the OT layer (MgO_6 octahedra and TO_4 tetrahedra) are, in turn, responsible for the rigidity of the b axis. Our pressure-dependent IR spectra of Ge-anhB (Fig. 7; supplementary Table 11) reveal that with increasing pressure there is a strong negative shift for vibrations v2 and v6, and a moderate negative shift for vibrations v1, v3, v4, and v5. A strong negative shift of OH bands indicates stronger compression in the direction of the corresponding OH dipole. The dipole involved in the v2 vibration should point toward the a - c plane, based on the strong response upon compression and our polarized IR spectra (Figs. 5 and 7), where v2 shows the highest intensity parallel to the c axis and a less intense contribution parallel to the a axis. This is consistent with the structure model suggested herein. Agreement of pressure data and polarized IR spectra is also obtained in the case of vibrations v1 and v4. Their moderate compressibility and polarization behavior (Fig. 5) suggests the OH dipoles point in the a - c direction, with v1 having a stronger a component than v4. According to the pleochroism observed for v3 the corresponding dipole is placed along the b axis. Under the terms of Crichton et al. (1999) the b axis is least compressible, which explains the intermediate response of v3 upon compression. The slightly higher displacement value of v3 compared to v1 and v4 can be explained by the fact that latter vibrations both have a component along a and c , which should lead to average total shifts. A comparison of the compressibility model with IR measurements for v6 is made difficult by the fact that this vibration exhibits very weak intensities in the polarized spectra.

The OH bands v5 and v6 and the weaker bands not labeled are most probably connected with Mg vacancies, because X-ray refinement indicates vacancies at the Mg2 to Mg5 sites. Applying the results of Crichton et al. (1999) vibrations v5 and v6 would point in the a/c or c direction, respectively and therefore might be coupled to MgO_6 octahedra of the O layer. A potential additional hydration site in Ge-anhB could be the O4 atom, as was previously proposed for anhB by Smyth (2006). This non-silicate oxygen has the lowest electrostatic potential in the structure. Combining all this information, we propose that v5 is most probably associated with a vacancy on the Mg5 site, and a charge-balancing proton bound to the coordinating O4 or O5 atom, whose $\text{O}\cdots\text{O}$ bond distance is 2.769 \AA . Since the charge-balancing of an octahedral Mg-vacancy requires two protons, we suggest the second proton is bound to either the O4 or O8 atom, whose $\text{O}\cdots\text{O}$ bond distance is 2.81 \AA , giving rise to vibration v6. The estimated hydrogen positions are in good agreement with the observed low-energy band positions of v5

and v6. However, we suggest that to gain further understanding of structural details of Ge-anhB, and to fully explain the IR spectra more work will be required.

We note a different trend in temperature-dependent spectra. All bands but v4 remain more-or-less at the same position, while v4 shifts to higher wavenumbers with decreasing temperature.

In conclusion, Ge-anhydrous phase B incorporates “water” differently than its silicate equivalent. Based on our data Ge-anhB is either an unsuitable analogue material for the equivalent mantle silicate, or the ability of silicate anhB to incorporate significant amounts of “water” has been simply overlooked in the past.

Ge-superhydrous phase B

By analogy to the Si-phase and based on its vibrational spectra, Ge-shyB has been refined in the acentric space group $Pnn2$ (Koch-Müller et al. 2005), which is supported by the symmetry analysis of the vibrational spectra. Infrared spectra of low-temperature Si-shyB as well as of Ge-shyB show the presence of two OH bands. Based on its composition, this can only be explained in an acentric space group. The correspondence of Ge-shyB with the silicate equivalent is also indicated by their vibrational signatures as a function of pressure. As observed by Koch-Müller et al. (2005), both OH bands in the Si-phase are very insensitive to changes in pressure, which is quite unusual for OH bands with band positions around 3350 cm^{-1} . For example, the OH band v3 (3360 cm^{-1}) in coesite, in the same pressure range, exhibits a shift of -68 cm^{-1} . Such a behavior is not observed for Ge-shyB. The stretching mode v1 (total shift -0.6 cm^{-1}) is almost insensitive to pressure, the OH stretching mode v2 displays a slight negative shift (-16 cm^{-1}) as function of pressure, which is reversible upon decompression, and indicates a small pressure-induced increase of the hydrogen bonding. The proposed atomic positions are chosen by analogy to the silicate (see Supplementary Table 8 and Koch-Müller et al. 2005).

Our data are interpreted as evidence that germanates are good low-pressure analogs for hydrous silicates with stoichiometrically incorporated water, since we observe an identical water concentration and incorporation mechanism for Ge-superhydrous phase B. The most important implication of this study is that germanates, though conveniently applicable as analogs for hydrous magnesium silicates, do not necessarily behave as strict analog materials for hydrogen defect studies of nominally anhydrous mantle silicates, as the concentration of “water” and the incorporation mechanism of “water” in nominally anhydrous phases depend on water fugacity and also on pressure and other intrinsic defects. A second point is the surprisingly high hydroxyl solubility observed in Ge-anhB. As a result of our study, there

is a possibility that anhB is able to store a significant amount of water, if present in the Earth's mantle as proposed by Ganguly and Frost (2006).

ACKNOWLEDGMENTS

We thank U. Schade and M. Schmidt for help with the synchrotron measurements at Bessy II in Berlin-Adlershof, and G. Berger for help with the preparation of single crystals. Useful comments by M. Gottschalk and W. Heinrich are gratefully appreciated. S.-M.T. thanks P. Davidson who kindly helped to improve the English. The suggestions and comments of two anonymous reviewers as well as A. Locock and E. Libowitzky significantly improved the manuscript.

REFERENCES CITED

- Akaogi, M. and Akimoto, S. (1986) Infrared spectra of high-pressure hydrous silicates in the system $\text{MgO-SiO}_2\text{-H}_2\text{O}$. *Physics and Chemistry of Minerals*, 13, 161–164.
- Altomare, A., Burla, M.C., Camalli, M., Cascarano, G.L., Giacovazzo, C., Guagliardi, A., Moliterni, A.G.G., Polidori, G., and Spagna, R. (1999) A new tool for crystal structure determination and refinement. *Journal of Applied Crystallography*, 32, 115–119.
- Armbruster, T. and Gnos, E. (2000) Tetrahedral vacancies and cation ordering in low-temperature Mn-bearing vesuvianites: Indication of a hydrogarnet-like substitution. *American Mineralogist*, 85, 570–577.
- Blanchard, M. and Wright, K. (2006) Defects associated with water in ringwoodite. "Water in Nominally Anhydrous Minerals," Abstract volume, 43. MSA Short Course, Verbania, Italy
- Blanchard, M., Wright, K., and Gale, J.D. (2005a) Atomistic simulation of Mg_2SiO_4 and Mg_2GeO_4 spinels: A new model. *Physics and Chemistry of Minerals*, 32, 332–338.
- (2005b) A computer simulation study of OH defects in Mg_2SiO_4 and Mg_2GeO_4 spinels. *Physics and Chemistry of Minerals*, 32, 585–593.
- Bolfan-Casanova, N., Keppler, H., and Rubie, D.C. (2000) Partitioning of water between mantle phases in the system $\text{MgO-SiO}_2\text{-H}_2\text{O}$ up to 24 GPa: Implications for the distribution of water in the Earth's mantle. *Earth and Planetary Science Letters*, 182, 209–221.
- Boyd, F.R. and England, J.L. (1960) Apparatus for phase-equilibrium measurements at pressures up to 50 kbar and temperatures up to 1740 °C. *Journal of Geophysical Research*, 65, 741–748.
- Chamorro-Pérez, E.M., Daniel, I., Chervin, J.-C., Dumas, P., Bass, J.D., and Inoue, T. (2006) Synchrotron IR study of hydrous ringwoodite ($\gamma\text{-Mg}_2\text{SiO}_4$) up to 30 GPa. *Physics and Chemistry of Minerals*, 33, 502–510.
- Chopelas, A., Boehler, R., and Ko, T. (1994) Thermodynamics and behavior of $\gamma\text{-Mg}_2\text{SiO}_4$ at high pressure: Implications for Mg_2SiO_4 phase equilibrium. *Physics and Chemistry of Minerals*, 21, 351–359.
- Crichton, W.A., Ross, N.L., and Gasparik, T. (1999) Equations of state of magnesium silicates anhydrous B and superhydrous B. *Physics and Chemistry of Minerals*, 26, 570–575.
- Cynn, H., Hofmeister, A.M., Burnley, P.C., and Navrotsky, A. (1996) Thermodynamic properties and hydrogen speciation from vibrational spectra of dense hydrous magnesium silicates. *Physics and Chemistry of Minerals*, 23, 361–376.
- Finger, L.W., Ko, J., Hazen, R.M., Gasparik, T., Hemley, R.J., Prewitt, C.T., and Weidner, D.J. (1989) Crystal chemistry of phase B and an anhydrous analogue: Implications for water storage in the upper mantle. *Nature*, 341, 140–142.
- Finger, L.W., Hazen, R.M., and Prewitt, C.T. (1991) Crystal structures of $\text{Mg}_{12}\text{Si}_4\text{O}_{19}(\text{OH})_2$ (phase B) and $\text{Mg}_{14}\text{Si}_5\text{O}_{24}$ (phase AnhB). *American Mineralogist*, 76, 1–7.
- Frost, D.J. (1999) The stability of dense hydrous magnesium silicates in Earth's transition zone and lower mantle. In Y. Fei, C.M. Bertka, and B.O. Mysen, Eds., *Mantle Petrology: Field Observations and High-Pressure Experimentation*. Geochemical Society, Special Publication No. 6, 283–295.
- Ganguly, J. and Frost, D.J. (2006) Stability of anhydrous phase B: Experimental studies and implications for phase relations in subducting slab and the X discontinuity in the mantle. *Journal of Geophysical Research*, 111, B06203.
- Gasparik, T. (1993) The role of volatiles in the transition zone. *Journal of Geophysical Research*, 98, 4287–4299.
- Guyot, F., Boyer, H., Madon, M., Velde, B. and Poirier, J.P. (1986) Comparison of the Raman microprobe spectra of $(\text{Mg,Fe})_2\text{SiO}_4$ and Mg_2GeO_4 with olivine and spinel structures. *Physics and Chemistry of Minerals*, 13, 91–95.
- Ibers, J.A. and Hamilton, W.C. (1974) *International Tables for X-ray Crystallography*, vol. IV, revised and supplementary tables. The Kynoch Press, Birmingham, U.K.
- Hertweck, B. and Ingrin, J. (2005) Hydrogen incorporation in a ringwoodite analogue: Mg_2GeO_4 spinel. *Mineralogical Magazine*, 69, 337–343.
- Herzberg, C. and Gasparik, T. (1989) Melting experiments on chondrite at high pressures: Stability of anhydrous phase B. *EOS, Transactions of the American Geophysical Union*, 70, 484.
- Hofmeister, A.M., Cynn, H., Burnley, P.C., and Meade, C. (1999) Vibrational spectra of dense, hydrous magnesium silicates at high pressure: Importance of the hydrogen bond angle. *American Mineralogist*, 84, 454–464.
- Inoue, T., Weidner, D.J., Northrup, P.A., and Parise, J.B. (1998) Elastic properties of hydrous ringwoodite (γ -phase) of Mg_2SiO_4 . *Earth and Planetary Science Letters*, 160, 107–113.
- Jeanloz, R. (1980) Infrared spectra of olivine polymorphs: α , β -phase and spinel. *Physics and Chemistry of Minerals*, 5, 327–339.
- Kanzaki, M. (1991) Stability of hydrous magnesium silicates in the mantle transition zone. *Physics of the Earth and Planetary Interiors*, 66, 307–312.
- Kato, T. and Kumazawa, M. (1985) Melting experiment on natural lherzolite at 20 GPa: Formation of phase B coexisting with garnet. *Geophysical Research Letters*, 13, 181–184.
- Kleppe, A.K., Jephcoat, A.P., and Smyth, J.R. (2002) Raman spectroscopic study of hydrous $\gamma\text{-Mg}_2\text{SiO}_4$ to 56.5 GPa. *Physics and Chemistry of Minerals*, 29, 473–476.
- Koch-Müller, M., Dera, P., Fei, Y., Reno, B., Sobolev, N., Hauri, E., and Wysoczanski, R. (2003) OH^- in synthetic and natural coesite. *American Mineralogist*, 88, 1436–1445.
- Koch-Müller, M., Dera, P., Fei, Y., Hellwig, H., Liu, Z., Van Orman, J., and Wirth, R. (2005) Polymorphic phase transition in superhydrous phase B. *Physics and Chemistry of Minerals*, 32, 349–361.
- Kohlstedt, D.L., Keppler, H., and Rubie, D.C. (1996) The solubility of water in α , β , and γ phases of $(\text{Mg,Fe})_2\text{SiO}_4$. *Contributions to Mineralogy and Petrology*, 123, 345–357.
- Kohn, S.C., Brooker, R.A., Frost, D.J., Slesinger, A.E., and Wood, B.J. (2002) Ordering of hydroxyl defects in hydrous wadsleyite ($\beta\text{-Mg}_2\text{SiO}_4$). *American Mineralogist*, 87, 293–301.
- Kudoh, Y., Kuribayashi, T., Mizohata, H., and Ohtani, E. (2000) Structure and cation disorder of hydrous ringwoodite, $\gamma\text{-Mg}_{1.88}\text{Si}_{0.97}\text{H}_{0.34}\text{O}_4$. *Physics and Chemistry of Minerals*, 27, 474–479.
- Lager, G.A., Armbruster, T., and Faber, J. (1987) Neutron and X-ray diffraction study of hydrogarnet $\text{Ca}_3\text{Al}_2(\text{O}_4\text{H})_2$. *American Mineralogist*, 72, 758–767.
- Lager, G.A., Armbruster, T., Rotella, F.J., and Rossman, G.R. (1989) OH substitution in garnets: X-ray and neutron diffraction, infrared, and geometric-modeling studies. *American Mineralogist*, 74, 840–851.
- Larson, A.C. and Von Dreele, R.B. (1987) Generalized structure analysis system (GSAS). Los Alamos National Laboratory Report No. LAUR 86-748.
- Libowitzky, E. (1999) Correlation of O-H stretching frequencies and O-H...O hydrogen bond lengths in minerals. *Monatshfte für Chemie*, 130, 1047–1059.
- Libowitzky, E. and Beran, A. (2006) The structure of hydrous species in nominally anhydrous minerals: Information from polarized IR spectroscopy. In H. Keppler and J.R. Smyth, Eds., *Water in Nominally Anhydrous Minerals*, 62, p. 29–52. *Reviews in Mineralogy and Geochemistry*, Mineralogical Society of America, Chantilly, Virginia.
- Libowitzky, E. and Rossman, G.R. (1997) An IR absorption calibration for water in minerals. *American Mineralogist*, 82, 1111–1115.
- Luth, R.W. (1993) Melting in the $\text{Mg}_2\text{SiO}_4\text{-H}_2\text{O}$ system at 3 to 12 GPa. *Geophysical Research Letters*, 20, 233–235.
- Mao, H.K. and Hemley, R.J. (1998) New windows on the Earth's deep interior. In R.J. Hemley, Ed., *Ultrahigh-pressure Mineralogy*, 37, p. 1–32. *Reviews in Mineralogy*, Mineralogical Society of America, Chantilly, Virginia.
- Mao, H.K., Xu, J., and Bell, P.M. (1986) Calibration of the ruby pressure gauge to 800 kbar under quasi-hydrostatic conditions. *Journal of Geophysical Research*, 91, 4673–4676.
- McMillan, P. and Akaogi, M. (1987) Raman spectra of $\beta\text{-Mg}_2\text{SiO}_4$ (modified spinel) and $\gamma\text{-Mg}_2\text{SiO}_4$ (spinel). *American Mineralogist*, 72, 361–364.
- Ohtani, E., Toma, M., Litasov, K., Kubo, T., and Suzuki, A. (2001) Stability of dense hydrous magnesium silicate phases and water storage capacity in the transition zone and lower mantle. *Physics of the Earth and Planetary Interiors*, 124, 105–117.
- Pacalo, R.E.G. and Parise, J.B. (1992) Crystal structure of superhydrous B, a hydrous magnesium silicate synthesized at 1400 °C and 20 GPa. *American Mineralogist*, 77, 681–684.
- Ringwood, A.E. (1975) *Composition and petrology of the Earth's mantle*, 618 p. McGraw-Hill, New York.
- Ringwood, A.E. and Major, A. (1967) High-pressure reconnaissance investigations in the system $\text{Mg}_2\text{SiO}_4\text{-MgO-H}_2\text{O}$. *Earth and Planetary Science Letters*, 2, 130–133.
- Ross, N.L. and Navrotsky, A. (1987) The Mg_2GeO_4 olivine-spinel phase transition. *Physics and Chemistry of Minerals*, 14, 473–481.
- Ross, N.L., Gibbs, G.V., and Rosso, K.M. (2003) Potential docking sites and positions of hydrogen in high-pressure silicates. *American Mineralogist*, 88, 1452–1459.
- Sheldrick, G.M. (1997) *SHELXL-97*, programs for crystal structure analysis, Release 97-2. University of Goettingen, Germany.
- Silver, P.G., Beck, S.L., Wallace, T.C., Meade, C., Myers, S.C., James, D.E., and Kuhnel, R. (1995) Rupture characteristics of the deep Bolivian earthquake of 9 June 1994 and the mechanism of deep-focus earthquakes. *Science*, 268,

- 69–73.
- Smyth, J.R. (1987) β - Mg_2SiO_4 : A potential host for water in the mantle? *American Mineralogist*, 72, 1051–1055.
- (2006) Hydrogen in high-pressure silicate and oxide mineral structures. In H. Keppler and J.R. Smyth, Eds., *Water in Nominally Anhydrous Minerals*, 62, p. 85–115. *Reviews in Mineralogy and Geochemistry*, Mineralogical Society of America, Chantilly, Virginia.
- Smyth, J.R., Kawamoto, T., Jacobsen, S.D., Swope, R.J., Hervig, R.L., and Holloway, J.R. (1997) Crystal structure of monoclinic hydrous wadsleyite [β -(Mg,Fe) $_2$ SiO $_4$]. *American Mineralogist*, 82, 270–275.
- Smyth, J.R., Holl, C.M., Frost, D.J., Jacobsen, S.D., Langenhorst, F., and McCammon, C.A. (2003) Structural systematics of hydrous ringwoodite and water in Earth's interior. *American Mineralogist*, 88, 1402–1407.
- Smyth, J.R., Holl, C.M., Frost, D.J., and Jacobsen, S.D. (2004) High pressure crystal chemistry of hydrous ringwoodite and water in the Earth's interior. *Physics of the Earth and Planetary Interiors*, 143–144, 271–278.
- Von Dreele, R.B., Bless, P.W., Kostiner, E., and Hughes, R.E. (1970) The crystal structure of magnesium germanate: A reformulation of Mg_2GeO_6 as $\text{Mg}_{28}\text{Ge}_{10}\text{O}_{48}$. *Journal of Solid State Chemistry*, 2, 612–618.
- Von Dreele, R.B., Navrotsky, A., and Bowman, A.L. (1977) Refinement of the crystal structure of Mg_2GeO_4 spinel. *Acta Crystallographica*, B33, 2287–2288.
- Wirth, R. (2004) Focused Ion Beam (FIB): A novel technology for advanced application of micro- and nanoanalysis in geosciences and applied mineralogy. *European Journal of Mineralogy*, 16, 863–876.
- X-RED (1996) Data Reduction Program, Stoe and Cie GmbH, Darmstadt, Germany.
- Yamamoto, K. and Akimoto, S. (1974) High-pressure and high-temperature investigations in the system $\text{MgO-SiO}_2\text{-H}_2\text{O}$. *Journal of Solid State Chemistry*, 9, 187–195.

MANUSCRIPT RECEIVED JULY 17, 2007

MANUSCRIPT ACCEPTED MARCH 24, 2008

MANUSCRIPT HANDLED BY EUGEN LIBOWITZKY

Table D1. Atomic coordinates ($\times 10^4$) and equivalent isotropic displacement parameters ($\text{\AA}^2 \times 10^3$) for Ge-ringwoodite and Ge-anhB. $U(\text{eq})$ is defined as one third of the trace of the orthogonalized U_{ij} tensor. Atomic positions of protons in Ge-anhB are given in Table 6.

	x	y	z	U (eq)
Ge-ringwoodite				
Ge	1250	1250	6250	20(2)
Mg	0	0	0	21(2)
O	2(6)	2(6)	7498(6)	22(2)
Ge-anhydrous				
Ge(1)	0	0	0	4(1)
Ge(2)	1256(1)	5016(1)	0	4(1)
Ge(3)	1863(1)	3250(1)	5000	6(1)
Mg(1)*	0	5000	5000	6(1)
Mg(2)*	0	0	5000	5(1)
Mg(3)*	1757(1)	1781(2)	0	6(1)
Mg(4)*	3260(1)	1463(2)	5000	6(1)
Mg(5)*	-44(1)	2517(1)	2423(2)	5(1)
Mg(6)*	3316(1)	4190(1)	2461(2)	6(1)
O(1)	836(3)	3380(4)	0	6(1)
O(2)	4218(3)	3481(4)	0	4(1)
O(3)	2518(3)	31(4)	0	7(1)
O(4)	686(3)	3299(4)	5000	5(1)
O(5)	4131(3)	3314(4)	5000	7(1)
O(6)	2565(3)	-220(4)	5000	6(1)
O(7)	756(2)	774(3)	2235(5)	5(1)
O(8)	4145(2)	812(3)	2485(5)	5(1)
O(9)	2427(2)	2509(3)	2723(5)	6(1)
Notes:	refined occupancies: Mg(1) 1.02(2); Mg(2) 0.99(2); Mg(3) 0.99(1); Mg(4) 0.98(1); Mg(5) 0.99(1);			
*	Mg(6) 0.99(1).			

Table D2. Bond lengths [\AA] and angles [$^\circ$] for Ge-Ringwoodite.

Ge-O(1)	1.782(9)
Ge-O	1.782(9)
Ge-O(2)	1.782(9)
Ge-O(3)	1.782(9)
Mg-O(4)	2.063(5)
Mg-O	2.063(5)
Mg-O(5)	2.063(5)
Mg-O(6)	2.063(5)
Mg-O(7)	2.063(5)
Mg-O(8)	2.063(5)
O(1)-Ge-O	109.5
O(1)-Ge-O(2)	109.471(1)
O-Ge-O(2)	109.5
O(1)-Ge-O(3)	109.471(1)
O-Ge-O(3)	109.471(1)
O(2)-Ge-O(3)	109.5
O(4)-Mg-O	89.9(3)
O(4)-Mg-O(5)	180.0
O-Mg-O(5)	90.1(3)
O(4)-Mg-O(6)	90.1(3)
O-Mg-O(6)	89.9(3)
O(5)-Mg-O(6)	89.9(3)
O(4)-Mg-O(7)	89.9(3)
O-Mg-O(7)	90.1(3)
O(5)-Mg-O(7)	90.1(3)
O(6)-Mg-O(7)	180.0
O(4)-Mg-O(8)	90.1(3)
O-Mg-O(8)	180.0
O(5)-Mg-O(8)	89.9(3)
O(6)-Mg-O(8)	90.1(3)
O(7)-Mg-O(8)	89.9(3)

Table D3. Anisotropic displacement parameters ($\text{\AA}^2 \times 10^3$) for $\gamma\text{-Mg}_2\text{GeO}_4$. The anisotropic displacement factor exponent takes the form: $-2p^2[h^2 a^* U^{11} + \dots + 2 h k a^* b^* U^{12}]$.

	U^{11}	U^{22}	U^{33}	U^{23}	U^{13}	U^{12}
Ge	20(2)	20(2)	20(2)	0	0	0
Mg	21(2)	21(2)	21(2)	-1(1)	-1(1)	-1(1)
O	22(2)	22(2)	22(2)	-2(2)	-2(2)	2(2)

Table D4. Selected bond lengths [Å] for Ge-anhB.

Ge(1)-O(7)	1.897(3)	Mg(3) -O(9)	2.030(4)
Ge(1)-O(7)	1.897(3)	Mg(3) -O(9)	2.030(4)
Ge(1)-O(7)	1.897(3)	Mg(3) -O(3)	2.104(5)
Ge(1)-O(7)	1.897(3)	Mg(3) -O(1)	2.113(5)
Ge(1)-O(2)	1.925(5)	Mg(3) -O(7)	2.223(4)
Ge(1)-O(2)	1.925(5)	Mg(3) -O(7)	2.223(4)
Ge(2)-O(3)	1.780(5)	Mg(4) -O(6)	1.995(5)
Ge(2)-O(1)	1.782(5)	Mg(4) -O(8)	2.082(4)
Ge(2)-(8)	1.784(3)	Mg(4) -O(8)	2.082(4)
Ge(2)-(8)	1.784(3)	Mg(4) -O(9)	2.108(4)
Ge(3)-(4)	1.710(5)	Mg(4) -O(9)	2.108(4)
Ge(3)-O(9)	1.754(3)	Mg(4) -O(5)	2.278(5)
Ge(3)-O(9)	1.754(3)	Mg(5) -O(4)	2.028(3)
Ge(3)-O(6)	1.772(5)	Mg(5) -O(2)	2.066(4)
Mg(1)-O(4)	2.006(5)	Mg(5) -O(8)	2.077(4)
Mg(1)-O(4)	2.006(5)	Mg(5) -O(1)	2.119(4)
Mg(1)-O(8)	2.114(4)	Mg(5) -O(5)	2.123(4)
Mg(1)-O(8)	2.114(4)	Mg(5) -O(7)	2.131(4)
Mg(1)-O(8)	2.114(4)	Mg(6) -O(6)	2.069(4)
Mg(1)-O(8)	2.114(4)	Mg(6) -O(3)	2.086(4)
Mg(2)-O(7)	2.130(4)	Mg(6) -O(2)	2.094(4)
Mg(2)-O(7)	2.130(4)	Mg(6) -O(7)	2.112(4)
Mg(2)-O(5)	2.138(5)	Mg(6) -O(5)	2.117(4)
Mg(2)-O(5)	2.138(5)	Mg(6) -O(9)	2.156(4)

Table D5. Selected angles [°] for Ge-anhB.

O(7)	Ge(1)	O(7)	91.0(2)	O(8)	Mg(1)	O(8)	90.08(19)	O(6)	Mg(4)	O(8)	92.07(15)
O(7)	Ge(1)	O(7)	89.0(2)	O(8)	Mg(1)	O(8)	89.92(19)	O(8)	Mg(4)	O(8)	91.9(2)
O(7)	Ge(1)	O(7)	180.0(2)	O(4)	Mg(1)	O(8)	87.19(13)	O(6)	Mg(4)	O(9)	98.51(16)
O(7)	Ge(1)	O(2)	90.27(14)	O(8)	Mg(1)	O(8)	89.92(19)	O(8)	Mg(4)	O(9)	168.10(14)
)	
O(7)	Ge(1)	O(2)	89.73(14)	O(8)	Mg(1)	O(8)	90.08(19)	O(8)	Mg(4)	O(9)	93.17(15)
O(2)	Ge(1)	O(2)	180.0(2)	O(8)	Mg(1)	O(8)	180.0	O(6)	Mg(4)	O(9)	98.51(16)
O(7)	Ge(1)	Mg(5)	46.08(9)	O(7)	Mg(2)	O(7)	180.0	O(9)	Mg(4)	O(9)	80.0(2)
O(3)	Ge(2)	O(1)	110.5(2)	O(7)	Mg(2)	O(7)	101.07(18)	O(6)	Mg(4)	O(5)	176.6(2)
O(3)	Ge(2)	O(8)	108.80(12)	O(7)	Mg(2)	O(7)	78.93(18)	O(8)	Mg(4)	O(5)	85.59(14)
O(1)	Ge(2)	O(8)	108.48(13)	O(7)	Mg(2)	O(7)	180.00(12)	O(9)	Mg(4)	O(5)	84.06(15)
O(8)	Ge(2)	O(8)	111.8(2)	O(7)	Mg(2)	O(5)	90.25(12)	O(4)	Mg(5)	O(2)	173.36(16)
)	
O(4)	Ge(3)	O(9)	118.60(13)	O(7)	Mg(2)	O(5)	89.75(12)	O(4)	Mg(5)	O(8)	87.63(17)
O(9)	Ge(3)	O(9)	101.0(2)	O(5)	Mg(2)	O(5)	180.0	O(2)	Mg(5)	O(8)	97.17(17)
O(4)	Ge(3)	O(6)	116.3(2)	O(9)	Mg(3)	O(9)	105.8(2)	O(4)	Mg(5)	O(1)	91.96(16)
O(9)	Ge(3)	O(6)	99.40(14)	O(9)	Mg(3)	O(3)	93.48(14)	O(2)	Mg(5)	O(1)	92.56(16)
O(4)	Mg(1)	O(4)	180.0	O(9)	Mg(3)	O(1)	91.10(14)	O(8)	Mg(5)	O(1)	90.64(17)
O(4)	Mg(1)	O(8)	87.19(13)	O(3)	Mg(3)	O(1)	172.40(19)	O(4)	Mg(5)	O(5)	84.71(16)
O(4)	Mg(1)	O(8)	92.81(13)	O(9)	Mg(3)	O(7)	163.74(13)	O(2)	Mg(5)	O(5)	90.71(15)
O(4)	Mg(1)	O(8)	87.19(13)	O(9)	Mg(3)	O(7)	90.36(15)	O(8)	Mg(5)	O(5)	89.81(17)
O(8)	Mg(1)	O(8)	180.00(13)	O(3)	Mg(3)	O(7)	87.07(16)	O(1)	Mg(5)	O(5)	176.62(13)
)	
O(4)	Mg(1)	O(8)	92.81(13)	O(1)	Mg(3)	O(7)	86.84(16)	O(4)	Mg(5)	O(7)	94.86(17)
O(7)	Mg(3)	O(7)	73.43(19)	O(9)	Mg(3)	O(7)	90.36(15)	O(2)	Mg(5)	O(7)	80.36(16)
O(9)	Mg(4)	O(5)	84.06(15)	O(3)	Mg(6)	O(9)	91.84(17)	O(8)	Mg(5)	O(7)	177.50(13)
)	
O(7)	Mg(6)	O(5)	90.77(17)	O(2)	Mg(6)	O(9)	98.57(16)	O(1)	Mg(5)	O(7)	89.09(17)
O(6)	Mg(6)	O(9)	79.06(16)	O(3)	Mg(6)	O(7)	90.52(17)	O(5)	Mg(5)	O(7)	90.60(17)
O(3)	Mg(6)	O(5)	178.47(16)	O(2)	Mg(6)	O(7)	79.74(16)	O(6)	Mg(6)	O(3)	91.87(16)

Table D6. Anisotropic displacement parameters ($\text{\AA}^2 \times 10^3$) for Ge-anhB. The anisotropic displacement factor exponent takes the form: $-2\pi^2 [h^2 a^{*2} U^{11} + \dots + 2 h k a^* b^* U^{12}]$.

	U ¹¹	U ²²	U ³³	U ²³	U ¹³	U ¹²
Ge(1)	5(1)	3(1)	5(1)	0	0	0(1)
Ge(2)	4(1)	4(1)	5(1)	0	0	0(1)
Ge(3)	6(1)	6(1)	6(1)	0	0	1(1)
Mg(1)	9(1)	3(1)	6(1)	0	0	2(1)
Mg(2)	6(2)	7(1)	3(1)	0	0	1(1)
Mg(3)	5(1)	6(1)	7(1)	0	0	-1(1)
Mg(4)	5(1)	4(1)	8(1)	0	0	1(1)
Mg(5)	6(1)	5(1)	4(1)	0(1)	0(1)	0(1)
Mg(6)	5(1)	7(1)	6(1)	1(1)	1(1)	0(1)
O(1)	9(2)	4(2)	6(2)	0	0	-1(1)
O(2)	5(2)	3(2)	5(2)	0	0	-1(1)
O(3)	9(2)	5(2)	7(2)	0	0	1(2)
O(4)	5(2)	5(2)	5(2)	0	0	-2(1)
O(5)	5(2)	8(2)	9(2)	0	0	0(2)
O(6)	5(2)	5(2)	9(2)	0	0	-1(1)
O(7)	6(1)	5(1)	4(1)	1(1)	-1(1)	0(1)
O(8)	6(1)	7(1)	3(1)	-3(1)	-1(1)	-2(1)
O(9)	6(1)	7(1)	6(1)	0(1)	1(1)	0(1)

Table D7. Rietveld results for Ge-shyB. Quality of refinement resembles trace amount of unidentified accessory phase.

phase	a (2 σ) [Å]	b (2 σ) [Å]	c (2 σ) [Å]	V (2 σ) [Å]	Wt (2 σ) fraction	W_{Rp}	Durbin-Watson	χ^2
Ge-shyB	14.202(1)	5.1676(2)	8.8756(4)	651.3(1)	0.80(0)	0.085	0.749	2.04
periclase	4.211(1)	4.211(1)	4.211(1)	74.70(2)	0.10(1)			
brucite	3.146(1)	3.146(1)	4.769(2)	40.87(2)	0.09(1)			

Table D8. Atomic coordinates for Ge-shyB.

	x	y	z
Ge1	0.000	0.000	-0.096(6)
Ge2	0.377(1)	0.012(2)	-0.092(6)
H1	0.300	0.600	0.100
H2	0.270	0.180	0.310
Mg(1)	0.174(2)	0.332(4)	-0.086(6)
Mg(2A)	0.174(3)	0.862(9)	0.086(6)
Mg(2B)	0.323(3)	0.334(9)	0.234(6)
Mg(3A)	0.000	0.500	0.732(8)
Mg(3B)	0.000	0.500	0.089(8)
Mg(4A)	0.000	0.000	0.567(9)
Mg(4B)	0.000	0.000	0.234(9)
O(1)	0.413(3)	0.680(8)	0.893(11)
O(2)	0.085(4)	0.685(8)	-0.113(9)
O(6)	0.253(3)	0.019(14)	-0.078(10)
O(3A)	0.257(4)	0.006(20)	0.244(10)
O(3B)	0.263(4)	0.506(18)	0.057(9)
O(4A)	0.067(5)	0.142(15)	0.068(9)
O(4B)	0.419(5)	0.647(16)	0.268(9)
O(5A)	0.408(4)	0.163(14)	0.069(9)
O(5B)	0.077(4)	0.695(14)	0.234(9)

Table D9. Selected bond lengths [\AA] for Ge-shyB.

Ge(1)-O(4B)	1.824(13)
Ge(1)-O(4A)	1.894(13)
Ge(1)-O(2)	2.031(7)
Ge(2)-O(5A)	1.689(12)
Ge(2)-O(5B)	1.919(12)
Ge(2)-O(6)	1.780(6)
Ge(2)-O(1)	1.796(7)
Mg(1)-O(6)	1.971(11)
Mg(1)-O(3A)	2.009(17)
Mg(1)-O(3B)	1.999(15)
Mg(1)-O(4B)	2.076(15)
Mg(2A)-O(3A)	1.965(16)
Mg(2A)-O(6)	1.994(13)
Mg(2A)-O(5B)	1.965(16)
Mg(2B)-O(3A)	1.959(17)
Mg(2B)-O(3B)	1.991(14)
Mg(3B)-O(5B)	1.980(14)
Mg(4A)-O(1)	2.180(15)
Mg(4A)-O(5A)	2.173(11)
Mg(4B)-O(5B)	1.924(11)
Mg(4B)-O(4A)	1.976(15)
Mg(4B)-O(1)	2.030(14)
O(3A)-H(2)	1.086(17)
O(3B)-H(1)	0.811(12)

Table D10. Band positions in the IR spectrum of Ge-ringwoodite as function of temperature.

Temperature [°C]	Band position [cm ⁻¹]				
25	3742	3688		3207	
-100	3751	3689	3350	3240	3150
-180	3758	3691	3345	3227	3138
Total shift 25 to -180 [cm ⁻¹]	+16	+3	-5	-13	-12

Table D11. Band positions in the IR spectrum of Ge-anhB as function of pressure.

Pressure [GPa]	Band position [cm^{-1}]					
	v1	v2	v3	v4	v5	v6
0.0	3621	3592	3582	3497	3418	3371
0.3	3620	3591	3581	3497	3417	3369
2.1	3618	3583	3577	3497	3417	3359
4.1	3618	3578	3563	3497	3416	3355
6.3	3614	3569		3498	3411	3345
7.9	3612	3568		3490	3411	3339
10.3	3612	3565		3486	3411	3332
Total shift [cm^{-1}]	-9	-27	-17	-11	-7	-39